Chemical Engineering Journal xxx (xxxx) xxxx

Contents lists available at ScienceDirect

Chemical Engineering Journal

journal homepage: www.elsevier.com/locate/cej

Novel core/void/shell composite phase change materials for high temperature thermal energy storage

Haiting Wei[a], Cuiping Wang[a,*], Shuiyuan Yang[a], Jiajia Han[a], Mujin Yang[a], Jinbin Zhang[a], Yong Lu[a], Xingjun Liu[b,c,d,*]

[a] College of Materials and Fujian Provincial Key Laboratory of Materials Genome, Xiamen University, Xiamen 361005, PR China
[b] State Key Laboratory of Advanced Welding and Joining, Harbin Institute of Technology, Shenzhen 518055, PR China
[c] Institute of Materials Genome and Big Data, Harbin Institute of Technology, Shenzhen 518055, PR China
[d] Shenzhen R&D Center for Al-based Hydrogen Hydrolysis Materials, Shenzhen 518055, PR China

HIGHLIGHTS

- A novel core (=Al-Si/Bi)/void/shell (=Al_2O_3) composite PCM was successfully prepared.
- The Al-Si alloy and Al_2O_3 shell were in-situ prepared by the displacement reaction.
- The void layer was formed by the evaporation of most of the outer Bi in Al/Bi alloy.
- The thermal stability of Al-Si/Bi/Al_2O_3 was obviously improved due to the void layer.
- The Al-Si/Bi/Al_2O_3 possessed an adjustable thermal energy storage performance.

ARTICLE INFO

Keywords:
Al-Si
Bi
Al_2O_3
Core/void/shell
Phase change thermal storage material

ABSTRACT

Metallic solid-liquid phase change materials (SLPCMs) are crucial for the thermal energy storage technology of various industrial systems. However, the encapsulation of metallic SLPCMs is still technically difficult. In this pursuit, the present research envisaged the development of a novel technology to successfully prepare the core (=Al-Si/Bi)/void/shell(=Al_2O_3) composite SLPCMs by using Al/Bi immiscible alloy powders as starting material and tetraethoxysilane as SiO_2 source. The Al-Si alloy and Al_2O_3 shell were in-situ synthesized by the displacement reaction between SiO_2 and molten Al. Interestingly, most of the Bi distributed in the shell of Al/Bi immiscible alloy powders could not only improve the activity of alloy powders and promote the formation of precursor shell, but also be recycled by evaporation to form the void layer during the calcination process of composite SLPCMs. The produced void layer provided a space buffer to alleviate the volume expansion of the core SLPCM, and thereby improving the thermal cycling stability of the prepared composite SLPCMs. The thermal cycling test results showed that after 300 thermal cycles, the melting latent heat reduction of the core (=Al-Si/Bi)/void/shell(=Al_2O_3) composite SLPCMs (24.3–31.7 J/g) was much less than that of the core(=Al-Si)/shell(=Al_2O_3) composite SLPCM (58.1 J/g). Moreover, the prepared Al-Si/Bi/Al_2O_3 exhibited an adjustable melting temperature (571.9 °C to 631.9 °C) and average particle diameter (39.3 μm to 112.6 μm), relatively high thermal conductivity [2.068 $W(mK)^{-1}$ to 2.966 $W(mK)^{-1}$], and excellent thermal energy storage capacity (209.5 J/g to 278.2 J/g). Thus, the prepared Al-Si/Bi/Al_2O_3 composite SLPCMs are potential thermal energy storage materials, which can be used to improve the energy efficiency of various industrial systems.

1. Introduction

With the rapid development in global industrialization, the problem of environmental pollution is getting worse and the energy crisis is becoming increasingly prominent [1–3]. Energy conservation and emission reduction are hence being given the top priority to achieve a sustainable development. It was reported that 80% of the energy utilization was associated with thermal energy and 45% of the energy was ultimately turned into waste heat [4,5]. Thus, the industrial waste heat recovery and utilization is an important way to achieve the goal of

* Corresponding authors at: College of Materials and Fujian Provincial Key Laboratory of Materials Genome, Xiamen University, Xiamen 361005, PR China (C. Wang).
E-mail addresses: wangcp@xmu.edu.cn (C. Wang), xjliu@hit.edu.cn (X. Liu).

https://doi.org/10.1016/j.cej.2019.123539
Received 28 July 2019; Received in revised form 18 October 2019; Accepted 17 November 2019

energy conservation and emission reduction. In recent years, the thermal energy storage technology using high temperature solid–liquid phase change materials (SLPCMs) has been widely studied in the waste heat recovery of various industrial systems [6–8].

Molten salts are the oldest and most studied high temperature SLPCMs due to their high thermal storage density [9–12]. However, a distinctive disadvantage of the molten salts SLPCMs is their poor thermal conductivity (Ex. $NaNO_3$: 0.56 $Wm^{-1}K^{-1}$) [13], which restricts their wide applications. Compared to molten salts, metals and alloys have a higher thermal conductivity (Ex. Cu: 393 $Wm^{-1}K^{-1}$) [14,15]. Therefore, more recently, metals and alloys have been extensively studied for new high temperature SLPCMs [16]. The encapsulation of metallic SLPCMs plays a very important role in their practical applications, which not only prevents the leakage of molten PCMs, but also protects the PCMs from the environmental reactions [17,18].

However, the encapsulation of metallic SLPCMs is still technically difficult owing to the following two problems [13,15]. Firstly, the molten metallic PCMs generally have a high chemical corrosion in the presence of shell materials. Therefore, the key requirement is to choose the suitable shell materials to encapsulate the metallic SLPCMs. Fernandez et al. [16] summarized that various oxides were the most promising shell materials of metallic SLPCMs, for e.g. Al_2O_3 was used for encapsulating Al-Si alloys [13,18,19] and SiOx was used for encapsulating Sn-Zn alloys [5]. Secondly, the volume expansion resulting from the phase transition was another challenge to be addressed in the encapsulation of solid–liquid PCMs, including metals and alloys [20–22]. In order to maintain the integrity of the core/shell structure during the phase transition process, it is necessary to design a void layer in the capsule for the volume expansion of core SLPCMs. From the above discussions, the development of core/void/shell composite SLPCM is indispensable to overcome the technology difficulties encountered in the encapsulation of metallic SLPCMs.

The noble metal particles/metal oxide shells are currently the most studied core/void/shell composite materials, and they find diverse applications in catalysis, medicine and biology due to their unique structure features and physicochemical properties [23]. However, these noble metal-based composites are not suitable for phase change thermal energy storage applications because noble metals generally have the characteristics of relatively high phase change temperature (e.g. Pt: 1768 °C, Au: 1064 °C), low thermal energy storage capacity and high cost. The Al and Al-based alloys are considered to be the most promising metallic SLPCMs due to their suitable phase change temperature range (e.g. Al: 660 °C, Al-Si alloys: 577 °C -660 °C), high thermal energy storage capacity (e.g. Al-12Si: 560 J/g) [8], great thermal stability and low cost (cost of Al: 2–4$/kg) [24]. Nevertheless, to the best of our knowledge, the research on the Al-based composite SLPCMs with core/void/shell structure is still in its infancy.

The template method is the most commonly used method for the synthesis of core/void/shell composite materials, and the desirable template should meet two requirements: (1) should be beneficial to combine the metal core with the target shell; (2) should be easily removable to produce the void layer [23]. Thus, the development of an effective and easily removable template has become the focus of research in the preparation of the core/void/shell Al-based composite SLPCMs. Wang and Liu [25] in our research group were the first authors to study the liquid phase separation and core/shell structure formation of the immiscible alloy powders prepared by gas atomization method. Since then, our research group has studied extensively the application of immiscible alloy powders [26–29]. More recently, Liu et. al [30] demonstrated the hydrogen generation property of the Al/Bi immiscible alloy powders. The research results showed that the low-melting-point phase Bi served as an activator to improve the activity of the alloy particles, and thereby increased the hydrogen production ability. Importantly, the low-melting-point phase Bi could be recycled by the evaporation of hydrogen generation products. Thus, the earlier reports indicated that the low-melting-point phase Bi in the immiscible alloy powders could meet the requirements of the template in the preparation of the core/void/shell Al-based composite SLPCMs, which inspired us to broaden the applications of immiscible alloy powders in the field of thermal energy storage.

In this study, we pioneered the use of Al/Bi immiscible alloy powders as starting material and tetraethoxysilane as the SiO_2 source to successfully prepare the novel core(=Al-Si/Bi)/void/shell(=Al_2O_3) composite SLPCMs, which opens up a new reference method for the encapsulation of metallic SLPCMs. Specifically, the Al-Si alloy and Al_2O_3 shell were in-situ synthesized by the displacement reaction between molten Al and SiO_2, and the void layer was generated from the evaporation of most of the outer Bi in the Al/Bi immiscible alloy powders. The produced void layer could provide a space buffer to alleviate the volume expansion of the core SLPCM, and thereby improving the thermal cycling stability of the prepared composite SLPCMs. The thermal cycling test results showed that after 300 thermal cycles, the melting latent heat reduction of the core(=Al-Si/Bi)/void/shell(=Al_2O_3) composite SLPCMs (24.3–31.7 J/g) was much less than that of the core(=Al-Si)/shell(=Al_2O_3) composite SLPCM (58.1 J/g).

2. Experimental

2.1. Materials

The Al/Bi (0at.%, 4at.%, 8at.%, 16at.% Bi) alloy powders used in this study were independently developed and prepared by our research group, and the specific preparation process was similar to the literature [30]. Polyvinylpyrrolidone (PVP, Analytical Reagent), 3-Aminopropyl trimethoxysilane (APTMS, Analytical Reagent), tetraethoxysilane (TEOS, Analytical Reagent), absolute ethanol (Analytical Reagent), and phenolic resin (PF, Analytical Reagent) were supplied by Sinopharm Chemical Reagent Company.

2.2. Preparation of the Al-Si/Bi/Al_2O_3 composite SLPCMs

The preparation process of Al-Si/Bi/Al_2O_3 composite SLPCMs was as follows: PVP (0.25 g) was dissolved in 100 mL of ethanol solution containing 95 mL absolute ethanol and 5 mL deionized water. 0.75 g of Al/Bi powders were added and then stirred at 50 °C for 0.5 h. APTMS (150 μL) was used as the coupling agent that was added dropwise into the solution and continuously stirred for 1 h. Subsequently, the mixed ethanol solution of TEOS and PF was carefully added into the above solution and maintained at 50 °C for 24 h. The samples were filtrated, dried, ground and calcined from room temperature to 600 °C and then at 1000 °C at a rate of 5 °C /min in an argon atmosphere. The holding time at 600 °C and 1000 °C was 0.5 h and 3 h, respectively. Finally, the products were calcined at 600 °C for 2 h in air atmosphere.

Fig. 1 shows the schematic diagram of the preparation process of Al-Si/Bi/Al_2O_3 composite SLPCMs. The preparation process of Al-Si/Bi/Al_2O_3 included two parts: the formation of composite precursor shell layer and the calcination in an argon atmosphere. The possible chemical reactions occurred in the formation of precursor shell layer are given in Section A of the Supporting information [31–33]. As given in Fig. 1, the thickness of precursor shell on the Al/Bi alloy particles can be adjusted by altering the addition amount of precursor TEOS or PF. In this study, we conducted the preparation processes by varying PF addition amounts (0.05 g, 0.075 g, 0.1 g) while maintaining the same TEOS weight (3.9 g). The prepared composite SLPCMs were named as $CP_{A\text{-}XB\text{-}Y}$, where X and Y represent the Bi atomic percentage of Al/Bi alloy powders and the mass ratio of precursor PF to alloy powders, respectively.

2.3. Characterization

The morphology observation and elemental analysis of the samples

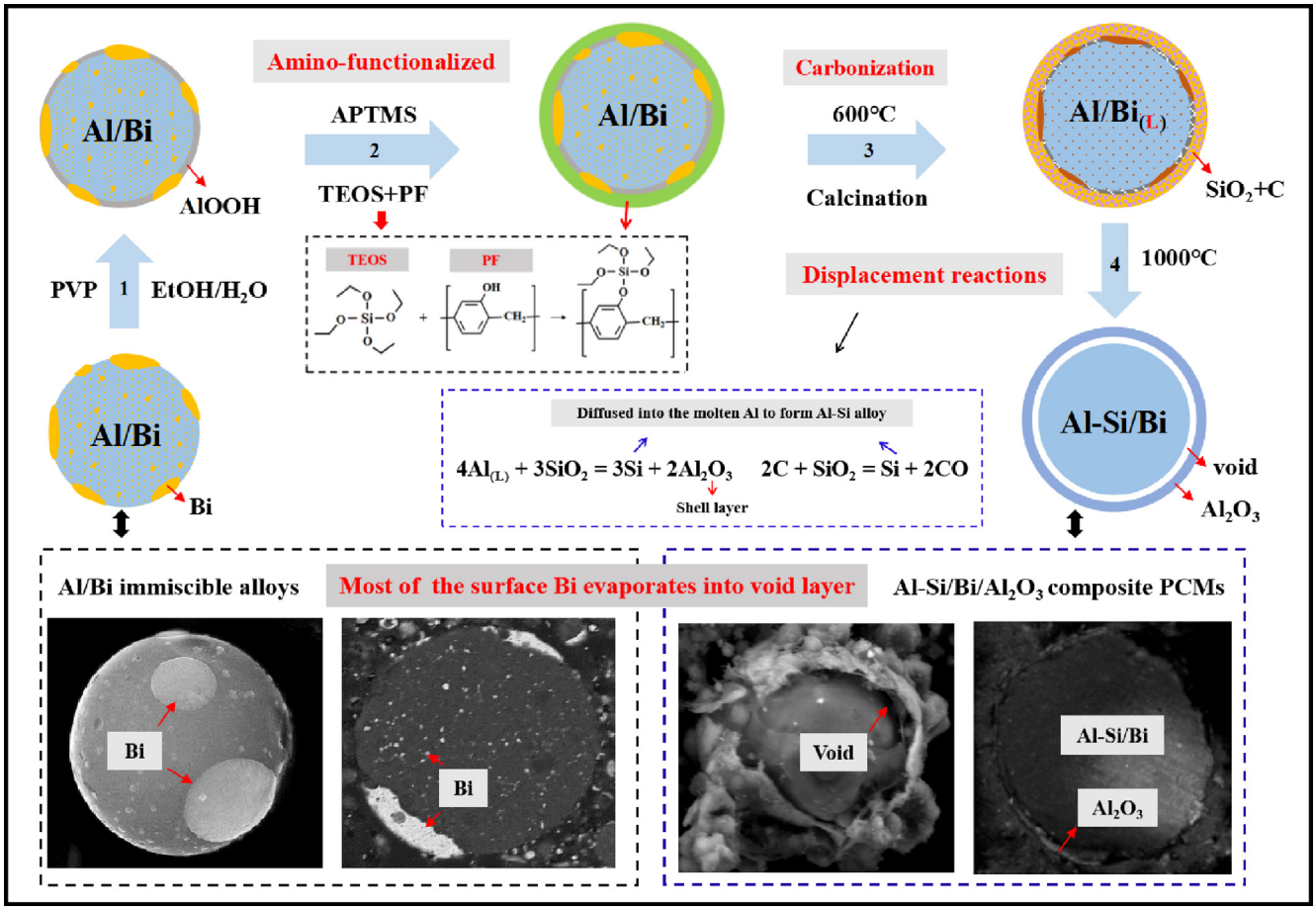

Fig. 1. Schematic diagram of the preparation process of Al-Si/Bi/Al_2O_3.

was performed using a scanning electron microscopy (SEM, SU-70) and energy dispersive spectroscopy (EDS), respectively. Without special explanation, the SEM images were all obtained under the acceleration voltage of 5 KV. The core/void/shell structure of the prepared composite SLPCMs was determined by the SEM image and elemental mappings of the cross-sectional sample. The formation of precursor shell layer was determined by a Fourier transform infrared spectrometer (FT-IR, Nicolet is10). The X-ray diffraction (XRD, D/MAX-Ultima IV) was used to assess the phase compositions of samples. The particle diameter distribution and average particle diameter of the prepared composite SLPCMs was examined via a laser particle analyzer (LS-POP9). The thermophysical properties of the prepared composite SLPCMs were studied by a differential scanning calorimetry (DSC, DSC404C) instrument. The thermal conductivity of the prepared composite SLPCMs was measured by a laser thermal conductivity testing instrument (LFA 447). The thermal stability and reusable performance of composite SLPCMs was characterized by 50, 100, 200 and 300 thermal cycling tests conducted in air.

3. Results and discussion

3.1. Structure characterization of the samples

The Al/4Bi alloy powders were considered to be not suitable as the starting material for preparing composite SLPCMs because they are relatively unstable and react easily with H_2O in the air [30,34], and the specific instructions can be found in Fig.S1-S3. The SEM images with different magnifications of Al/0Bi, Al/8Bi and Al/16Bi alloy powders are presented in Fig. 2. The Al/0Bi powders were spherical with a smooth surface and possessed obvious grain boundaries on the powder surface [Fig. 2 (a, a1)]. According to Fig. 2 (b, b1) and the SEM image of cross-sectional Al/8Bi alloy (Fig.S4), most of the low melting point phases Bi (the white spherical spots) distributed in the shell and a few of them distributed in the core. This morphology formation was ascribed to the combined effects of two immiscible liquid phases (Al-rich and Bi-rich) fraction, Stokes and Marangoni velocities of the droplets, and the Al/Bi alloy sample rotation direction during the solidification process. Thus, to lower the whole droplet energy, the Bi-rich phases with lower interfacial energy moved to the droplet surface to form a shell layer, while the Al-rich phases were distributed in the core of droplet. However, owing to the large density of Bi, the volume of the Bi-rich phase was too small to form a complete shell layer, which resulted in the distribution of the Bi-rich phase on powder surface in the form of spherical spots [25,30]. When the atomic percentage of Bi increased to 16%, the volume of the Bi-rich shell layer obviously increased in the Al/16Bi alloy particles [Fig. 2 (c, c1)].

Fig. 2 (d-f) shows the SEM images of $CP_{A\text{-}0B\text{-}0.13}$, $CP_{A\text{-}8B\text{-}0.13}$ and $CP_{A\text{-}16B\text{-}0.13}$ at a low magnification. It is clearly observed that most of the Al/0Bi, Al/8Bi and Al/16Bi alloy powders retained their original shapes after microencapsulation. To observe the surface morphology of samples more clearly, the SEM images with a high magnification of $CP_{A\text{-}0B\text{-}0.13}$, $CP_{A\text{-}8B\text{-}0.13}$ and $CP_{A\text{-}16B\text{-}0.13}$ are shown in Fig. 2 (d1), (e1) and (f1), respectively. As given in Fig. 2 (d1), the sample $CP_{A\text{-}0B\text{-}0.13}$ showed a rough surface with many small particles. The surfaces of samples $CP_{A\text{-}8B\text{-}0.13}$ [Fig. 2 (e1)] and $CP_{A\text{-}16B\text{-}0.13}$ [Fig. 2 (f1)] were relatively smooth and continuous. Moreover, the element composition of $CP_{A\text{-}0B\text{-}0.13}$, $CP_{A\text{-}8B\text{-}0.13}$ and $CP_{A\text{-}16B\text{-}0.13}$ was determined by EDS and the analysis results are given in Table 1. The energy dispersion spectrometer can only detect the element composition of samples several micrometers below the surface. Therefore, the EDS analysis results of the prepared composite

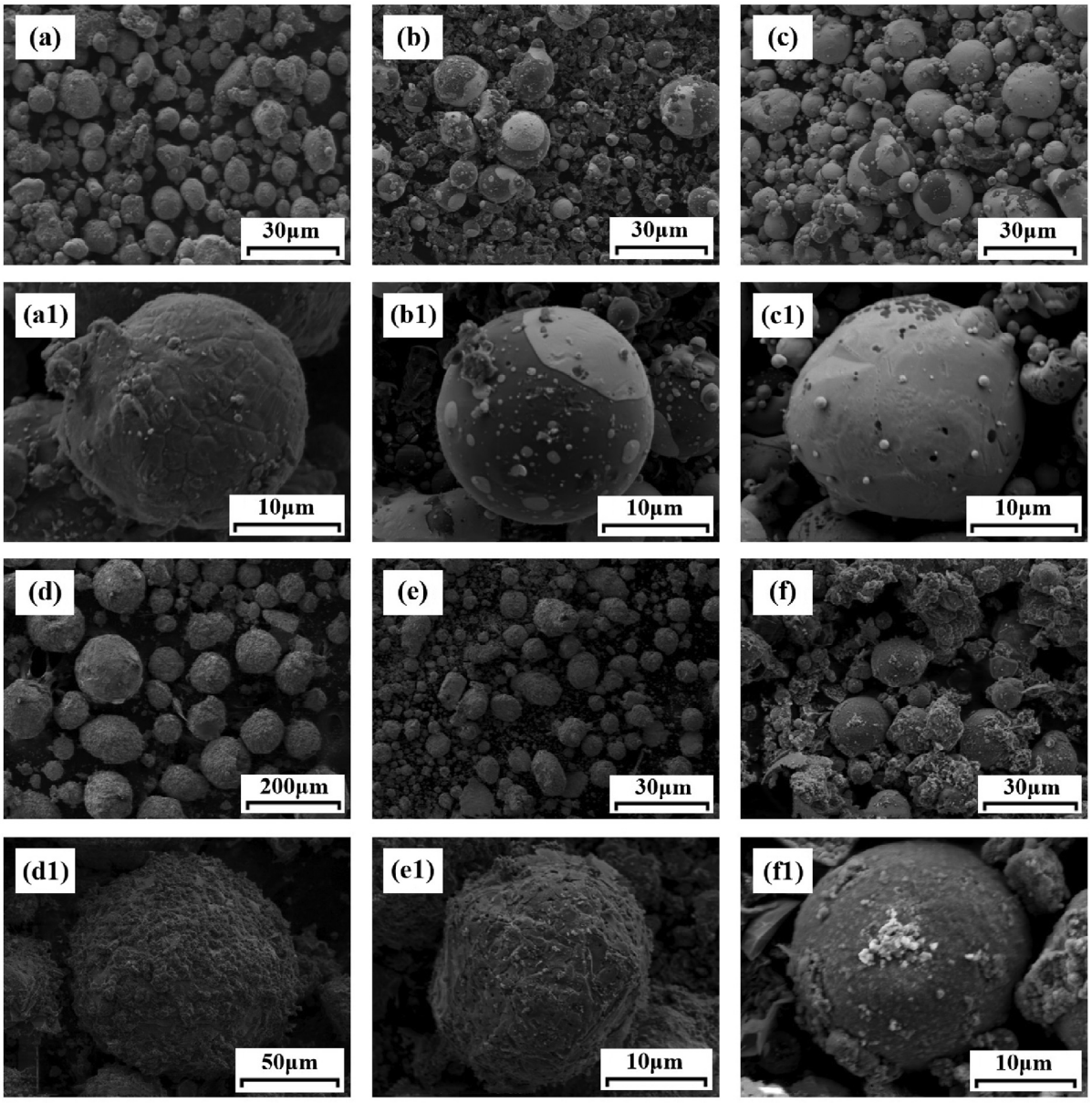

Fig.2. SEM images with different magnifications of (a, a1) Al/0Bi; (b, b1) Al/8Bi; (c, c1) Al/16Bi; (d, d1) $CP_{A\text{-}0B\text{-}0.13}$; (e, e1) $CP_{A\text{-}8B\text{-}0.13}$ and (f, f1) $CP_{A\text{-}16B\text{-}0.13}$.

Table 1
Elemental composition of $CP_{A\text{-}0B\text{-}0.13}$, $CP_{A\text{-}8B\text{-}0.13}$ and $CP_{A\text{-}16B\text{-}0.13}$.

Element	$CP_{A\text{-}0B\text{-}0.13}$ (at.%)	$CP_{A\text{-}8B\text{-}0.13}$ (at.%)	$CP_{A\text{-}16B\text{-}0.13}$ (at.%)
O	51.65	50.45	53.04
Al	46.95	44.81	39.33
Si	1.40	4.31	5.91
Bi	–	0.43	1.72
Total	100.00	100.00	100.00

SLPCMs mainly reflected the elemental composition of the shell layer. According to Table 1, the shell layer of $CP_{A\text{-}0B\text{-}0.13}$, $CP_{A\text{-}8B\text{-}0.13}$ and $CP_{A\text{-}16B\text{-}0.13}$ was mainly composed of Al and O elements. To observe the shell layer elemental distribution more visually, the elemental mappings of the prepared composite SLPCMs (i.e., the sample $CP_{A\text{-}8B\text{-}0.13}$) are presented in Fig.S5.

The SEM images and elemental mappings of cross-sectional $CP_{A\text{-}0B\text{-}0.13}$, $CP_{A\text{-}8B\text{-}0.13}$, $CP_{A\text{-}16B\text{-}0.13}$ were used to further detect the inner structure, as given in Fig.S6, Fig. 3 and Fig.S7. As seen from Fig.S6, a core/shell structure was observed in sample $CP_{A\text{-}0B\text{-}0.13}$ and the core was made up of Al and Si elements, while the O element was mainly distributed in the shell layer. According to Fig. 3 (a), a void layer was seen between the core and the shell, and the generation of void layer can be ascribed to the evaporation of most of the outer Bi in Al/Bi alloy powders. Fig. 3 (b-e) shows that the core of particle was principally composed of Al, Si and Bi elements. The O element was mainly distributed in the shell layer of sample $CP_{A\text{-}8B\text{-}0.13}$ and the distribution was relatively continuous and uniform. Furthermore, the SEM image of cracked $CP_{A\text{-}8B\text{-}0.13}$ [Fig. 3 (f)] also proved the formation of a core/void/shell structure. A further elaboration can be made that due to the low solubility of Bi with Al and Si, the low melting point phase Bi usually existed in the Al-Si alloy matrix as an independent phase. The similar core/void/shell structure was detected in the sample $CP_{A\text{-}16B\text{-}0.13}$ (Fig.S7). However, the raw material cost is an important factor to be considered in the actual manufacture. The Al/8Bi alloy powders are more economical than the Al/16Bi alloy powders, because the price of Al is lower than that of Bi. In summary, the Al/8Bi alloy powders are the most promising starting material for preparing the composite

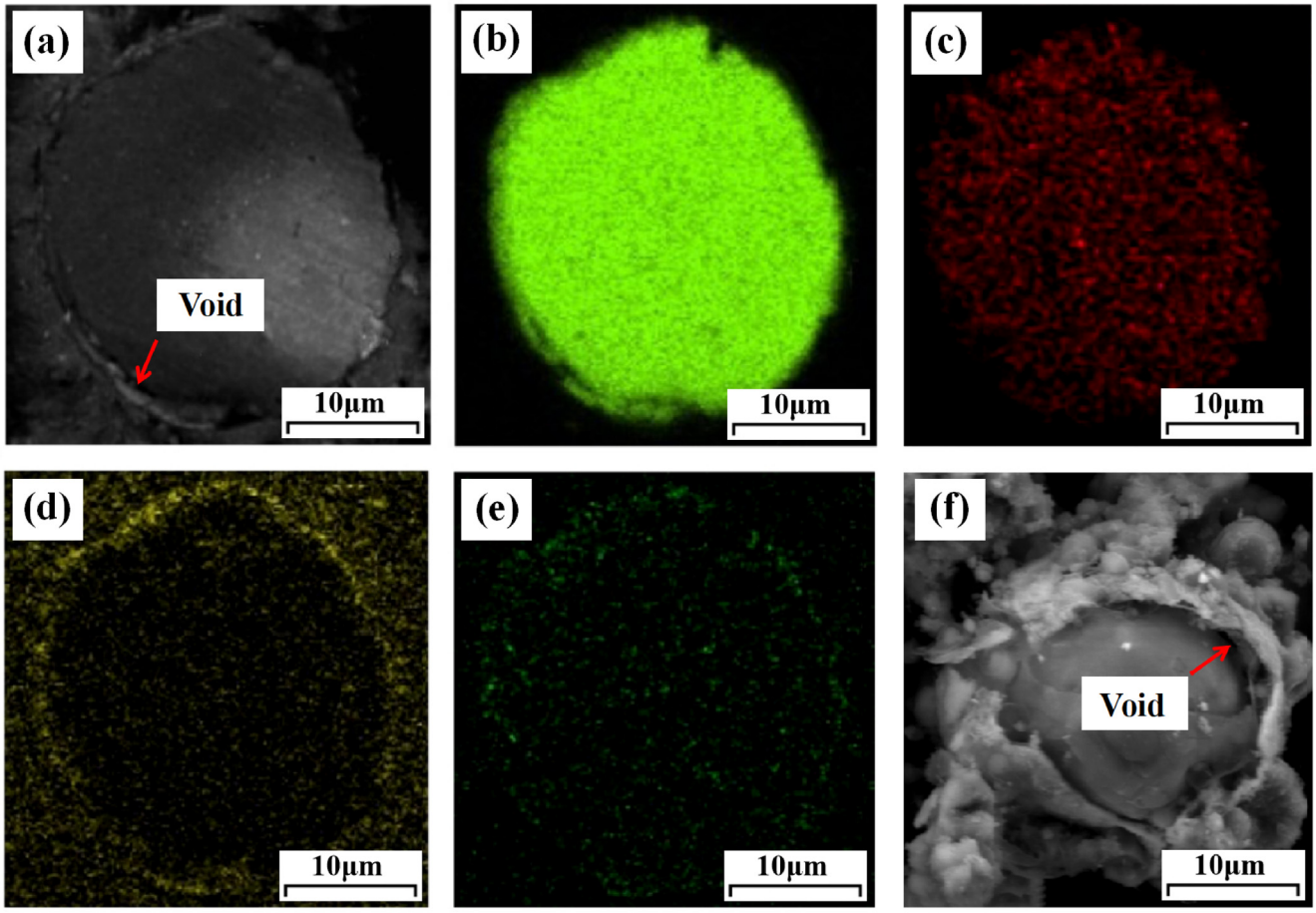

Fig. 3. (a) SEM image and (b) Al element mapping; (c) Si element mapping; (d) O element mapping; (e) Bi element mapping of cross-sectional $CP_{A\text{-}8B\text{-}0.13}$; (f) SEM image of cracked $CP_{A\text{-}8B\text{-}0.13}$.

SLPCMs among the four Al/Bi alloy powders. To demonstrate the alloy composition adjustability of the composite SLPCMs, we selected the Al/8Bi alloy as the starting material and prepared three composite SLPCMs with different raw material mass rations ($CP_{A\text{-}8B\text{-}0.07}$, $CP_{A\text{-}8B\text{-}0.10}$ and $CP_{A\text{-}8B\text{-}0.13}$). The SEM images with different magnifications of the prepared $CP_{A\text{-}8B\text{-}0.07}$, $CP_{A\text{-}8B\text{-}0.10}$ and $CP_{A\text{-}8B\text{-}0.13}$ are shown in Fig.S8. Moreover, the SEM images of cracked samples $CP_{A\text{-}8B\text{-}0.07}$, $CP_{A\text{-}8B\text{-}0.10}$ and $CP_{A\text{-}8B\text{-}0.13}$ are also given in Fig.S8 (c), (f) and (i), respectively.

The FT-IR spectra of $CP_{A\text{-}0B\text{-}0.13}$, $CP_{A\text{-}8B\text{-}0.07}$, $CP_{A\text{-}8B\text{-}0.10}$ and $CP_{A\text{-}8B\text{-}0.13}$ before calcination were given in Fig. 4 (a). As seen from Fig. 4 (a), the peak at 1057 cm^{-1} was attributed to the Si-O stretching vibration [35,36], which was originated from the hydrolysis and condensation of raw material TEOS. The C = C stretching vibration peak of the benzene ring was observed at 1652 cm^{-1} [37,38]. Moreover, the peaks intensities of Si-O and C = C in the prepared composite SLPCMs obviously increased with the increase of the raw material mass ratio, as given in Fig. 4 (a). By comparing the FT-IR spectra of $CP_{A\text{-}0B\text{-}0.13}$ and $CP_{A\text{-}8B\text{-}0.13}$, it was found that there was no obvious difference in the peak position and shape of the spectra, but the characteristic peaks intensities of Si-O and C = C in sample $CP_{A\text{-}8B\text{-}0.13}$ significantly increased. This suggests that during the formation process of precursor shell, the low melting point phase Bi did not participate in the reaction, but acted as an additive to promote the reaction between Al and H_2O to produce Al-OH groups [29,30]. The Al-OH groups are conducive to the amination of Al/Bi microspheres surface and the formation of precursor shell [39].

The XRD patterns of Al/8Bi, $CP_{A\text{-}0B\text{-}0.13}$, $CP_{A\text{-}8B\text{-}0.07}$, $CP_{A\text{-}8B\text{-}0.10}$ and $CP_{A\text{-}8B\text{-}0.13}$ were given in Fig. 4 (b). According to the XRD pattern of $CP_{A\text{-}0B\text{-}0.13}$, the phase composition of sample $CP_{A\text{-}0B\text{-}0.13}$ was Al and a small amount of Al_2O_3, Si. The Al_2O_3 and Si phases were derived from the displacement reaction between Al and SiO_2 ($4Al + 3SiO_2 = 3Si + 2Al_2O_3$) [40–43]. Compared to sample $CP_{A\text{-}0B\text{-}0.13}$, the intensities of Si and Al_2O_3 diffraction peaks in sample $CP_{A\text{-}8B\text{-}0.13}$ increased markedly. As seen from Fig. 4 (b), the samples $CP_{A\text{-}8B\text{-}0.07}$, $CP_{A\text{-}8B\text{-}0.10}$ and $CP_{A\text{-}8B\text{-}0.13}$ were made up of Al, Bi, Al_2O_3 and Si phases. The intensities of Si and Al_2O_3 diffraction peaks increased with the increase of the raw material mass ratio, which were closely related to the loaded amount of the composite precursor shell layer produced by TEOS (SiO_2 source) and PF. Furthermore, the Bi diffraction peaks intensities of the prepared composite SLPCMs were much lower than those of the Al/8Bi alloy powders. This is attributed to that during the preparation process of composite SLPCMs, the calcination temperature (1000 °C) was much higher than the melting point of metal Bi (~271 °C), thereby resulting in the evaporation of most of the Bi. In conclusion, according to the analysis results of SEM, EDS and XRD, the prepared Al-Si/Bi/Al_2O_3 composite SLPCMs exhibited a core/void/shell structure. Specifically, the core was composed of Al-Si alloy and Bi phases, and the shell layer was mainly made up of Al_2O_3 phase.

The particle diameter distribution diagrams and the average particle diameter of $CP_{A\text{-}0B\text{-}0.13}$, $CP_{A\text{-}8B\text{-}0.07}$, $CP_{A\text{-}8B\text{-}0.10}$ and $CP_{A\text{-}8B\text{-}0.13}$ are presented in Fig. 5. As shown in Fig. 5 (a), the particle diameter distributions of $CP_{A\text{-}0B\text{-}0.13}$, $CP_{A\text{-}8B\text{-}0.07}$, $CP_{A\text{-}8B\text{-}0.10}$ and $CP_{A\text{-}8B\text{-}0.13}$ were close to the normal distribution, indicating that the particle diameter distribution of the prepared composite SLPCMs was relatively uniform. According to Fig. 5 (b), the average particle diameter of $CP_{A\text{-}0B\text{-}0.13}$, $CP_{A\text{-}8B\text{-}0.07}$, $CP_{A\text{-}8B\text{-}0.10}$ and $CP_{A\text{-}8B\text{-}0.13}$ was 131.3 μm, 112.6 μm, 67.8 μm and 39.3 μm, respectively. By comparing the average particle diameter of $CP_{A\text{-}8B\text{-}0.07}$, $CP_{A\text{-}8B\text{-}0.10}$ and $CP_{A\text{-}8B\text{-}0.13}$, it can be concluded that the

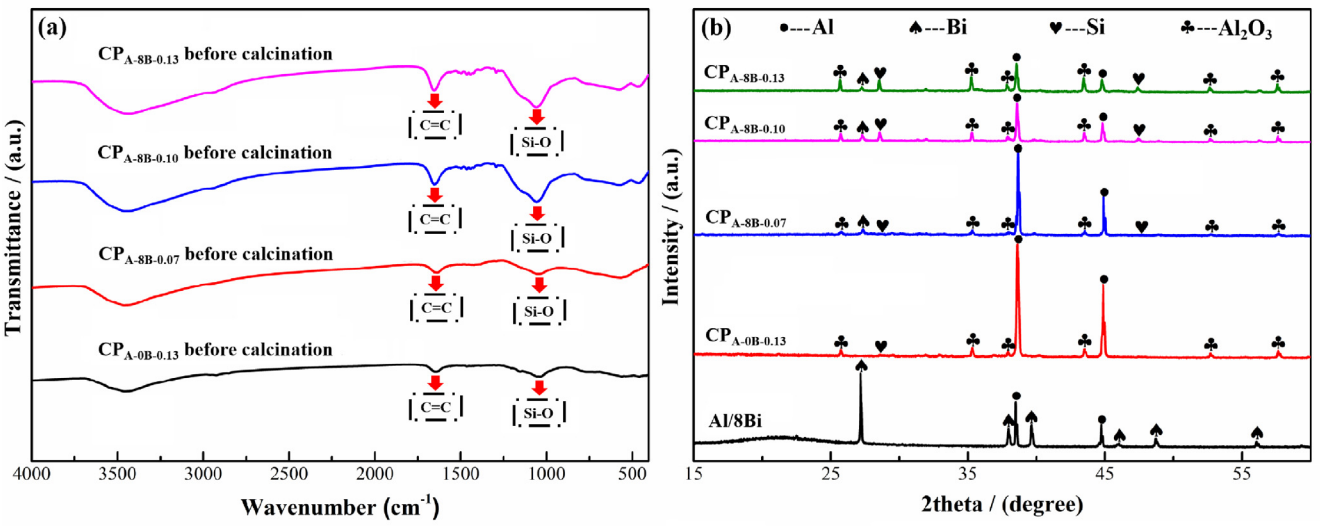

Fig. 4. (a) FT-IR spectra of $CP_{A\text{-}0B\text{-}0.13}$; $CP_{A\text{-}8B\text{-}0.07}$; $CP_{A\text{-}8B\text{-}0.10}$ and $CP_{A\text{-}8B\text{-}0.13}$ before calcination, (b) XRD patterns of Al/8Bi; $CP_{A\text{-}0B\text{-}0.13}$; $CP_{A\text{-}8B\text{-}0.07}$; $CP_{A\text{-}8B\text{-}0.10}$ and $CP_{A\text{-}8B\text{-}0.13}$.

particle diameter of the prepared composite SLPCMs increased with the decrease in the raw material mass ratio. This phenomena can be explained as follows. During the calcination process, the produced thin precursor shell layer attributed to the small amount of precursor TEOS and PF loaded on the microspheres surface, could not resist the thermal stress due to the volume expansion of core PCM melting, thereby resulting in the partial shell cracking and particle coarsening. Additionally, the average particle diameter of $CP_{A\text{-}8B\text{-}0.13}$ (39.3 μm) was much smaller than that of $CP_{A\text{-}0B\text{-}0.13}$ (131.3 μm), which was ascribed to the increased activation of alloy powders that promoted the reaction between Al and H_2O to produce Al-OH groups, thus benefiting the amination of Al/Bi microspheres surface and the formation of precursor shell [29,30].

3.2. Thermal storage property of the prepared composite SLPCMs

The phase change temperature and latent heat of composite SLPCMs are two significant parameters of thermal storage property. The phase change temperature includes the melting temperature and crystallization temperature, which respectively correspond to the latent heat storage and release temperature. Thus, the phase change temperature of composite SLPCMs largely determines their practical working conditions. The phase change latent heat, which is calculated by the integral area of endothermic or exothermic peak, is the common index to evaluate the effect of the thermal storage or release of composite SLPCMs. In this study, the phase change temperature and latent heat of the prepared composite SLPCMs were obtained from the DSC heating and cooling curves.

Fig. 6 shows the DSC curves of $CP_{A\text{-}0B\text{-}0.13}$, $CP_{A\text{-}8B\text{-}0.07}$, $CP_{A\text{-}8B\text{-}0.10}$ and $CP_{A\text{-}8B\text{-}0.13}$, and Table 2 lists the melting temperature, melting latent heat, crystallization temperature and crystallization latent heat of the prepared composite SLPCMs. Two endothermic peaks were observed corresponding to the eutectic and alloy melting, respectively, in the DSC heating curves of $CP_{A\text{-}0B\text{-}0.13}$, $CP_{A\text{-}8B\text{-}0.07}$ and $CP_{A\text{-}8B\text{-}0.10}$. Only an endothermic peak was seen in the DSC heating curve of sample $CP_{A\text{-}8B\text{-}0.13}$. Moreover, with the increase of the raw material mass ratio, the secondary endothermic peak resulted from alloy melting shifts toward a lower temperature along with an increase in the intensity of primary endothermic peak. It can be seen from Table 2 that the melting temperature and crystallization temperature of $CP_{A\text{-}8B\text{-}0.07}$, $CP_{A\text{-}8B\text{-}0.10}$ and $CP_{A\text{-}8B\text{-}0.13}$ can be tuned from 571.9 °C to 631.9 °C and 568.2 °C to 637.4 °C, respectively. The reason for the adjustability of phase change temperature in the prepared composite SLPCMs can be demonstrated as follows. In the prepared composite SLPCMs, the Al-Si binary alloy was

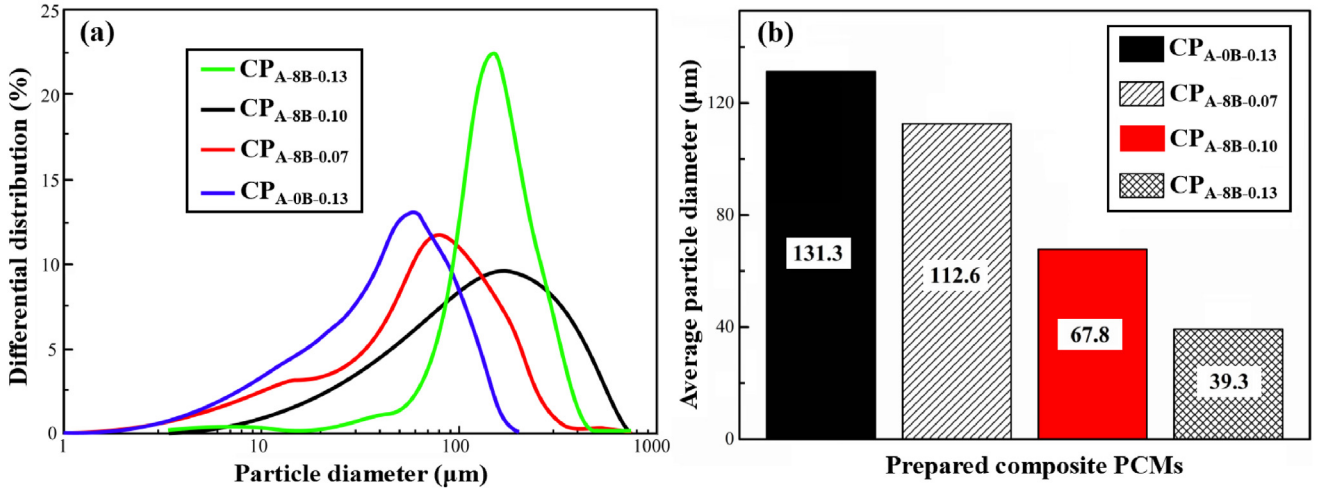

Fig. 5. (a) Particle diameter distribution diagrams and (b) average particle diameter of $CP_{A\text{-}0B\text{-}0.13}$; $CP_{A\text{-}8B\text{-}0.07}$; $CP_{A\text{-}8B\text{-}0.10}$ and $CP_{A\text{-}8B\text{-}0.13}$.

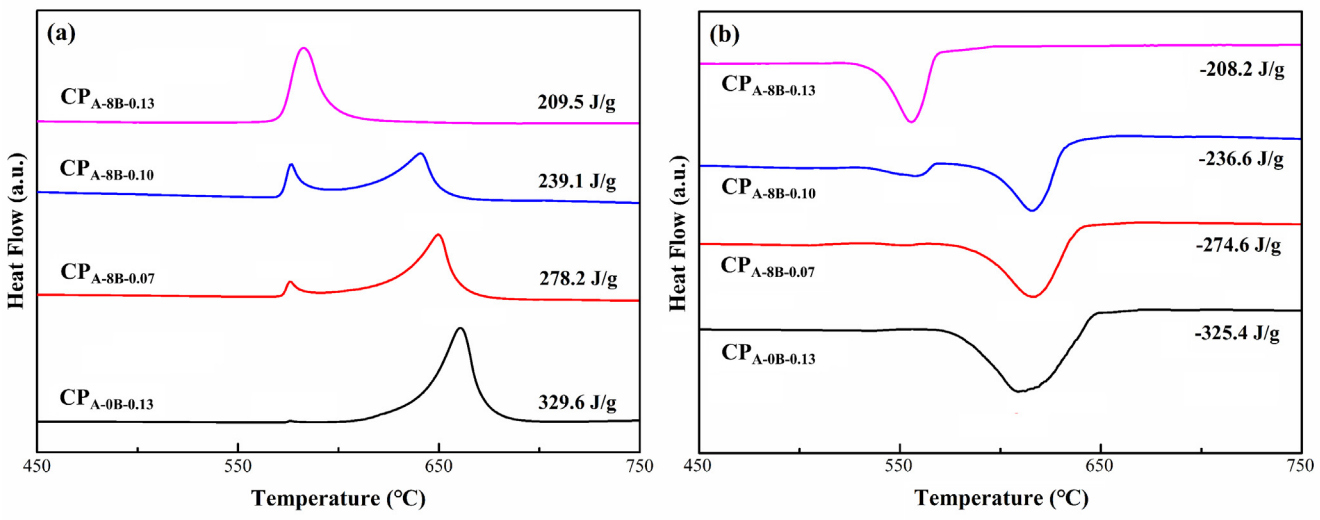

Fig. 6. DSC (a) heating curves; (b) cooling curves of $CP_{A\text{-}0B\text{-}0.13}$, $CP_{A\text{-}8B\text{-}0.07}$, $CP_{A\text{-}8B\text{-}0.10}$ and $CP_{A\text{-}8B\text{-}0.13}$.

Table 2
Thermophysical properties of samples $CP_{A\text{-}0B\text{-}0.13}$, $CP_{A\text{-}8B\text{-}0.07}$, $CP_{A\text{-}8B\text{-}0.10}$ and $CP_{A\text{-}8B\text{-}0.13}$.

Samples	Melting temperature (°C)	Crystallization temperature (°C)	Melting latent heat (J/g)	Crystallization latent heat (J/g)
$CP_{A\text{-}0B\text{-}0.13}$	573.8/641.2	646.1	329.6	−325.4
$CP_{A\text{-}8B\text{-}0.07}$	572.4/631.9	637.4	278.2	−274.6
$CP_{A\text{-}8B\text{-}0.10}$	571.8/623.1	567.0/631.7	239.1	−236.6
$CP_{A\text{-}8B\text{-}0.13}$	571.9	568.2	209.5	−208.2

used as the SLPCM matrix, which results in that the phase change temperature of the prepared composite SLPCMs largely depends on that of Al-Si binary alloys. According to the binary phase diagram of Al-Si alloy (Fig.S9), the phase change temperature of Al-Si binary alloy is closely related to the component of Al-Si alloy, and the melting or crystallization process of binary alloy is within a certain temperature range (from the eutectic melting temperature to liquidus temperature), rather than at a specific temperature. Furthermore, the liquidus temperature of Al-Si binary alloy varied with the Si content in the system, as given in Fig.S9. Thus, the phase change temperatures of the prepared composite SLPCMs can be altered by adjusting the Si content in the system. Meanwhile, the Si content of samples $CP_{A\text{-}0B\text{-}0.13}$, $CP_{A\text{-}8B\text{-}0.07}$, $CP_{A\text{-}8B\text{-}0.10}$ and $CP_{A\text{-}8B\text{-}0.13}$ can be reckoned by the liquidus temperature. According to Fig. 6 and Table 2, the liquidus temperature of $CP_{A\text{-}0B\text{-}0.13}$, $CP_{A\text{-}8B\text{-}0.07}$ and $CP_{A\text{-}8B\text{-}0.10}$ was 641.2 °C, 631.9 °C and 623.1 °C, respectively. There is an endothermic peak was detected in the DSC heating curve of sample $CP_{A\text{-}8B\text{-}0.13}$, indicating that the Si content of sample $CP_{A\text{-}8B\text{-}0.13}$ was close to that of Al-Si eutectic alloy (11.7% Si). To further reckon the Si content of $CP_{A\text{-}8B\text{-}0.13}$, the peak melting temperature of endothermic peak (582.1 °C) was taken as the liquidus temperature [44]. Therefore, the Si content of the prepared $CP_{A\text{-}0B\text{-}0.13}$, $CP_{A\text{-}8B\text{-}0.07}$, $CP_{A\text{-}8B\text{-}0.10}$ and $CP_{A\text{-}8B\text{-}0.13}$ can be estimated to be around 2.65%, 3.96%, 5.20% and 10.98%, respectively.

As listed in Table 2, the melting and crystallization latent heat range of $CP_{A\text{-}8B\text{-}0.07}$, $CP_{A\text{-}8B\text{-}0.10}$ and $CP_{A\text{-}8B\text{-}0.13}$ was 209.5–278.2 J/g and 208.2–274.6 J/g, respectively. Moreover, the phase change latent heat of composite SLPCMs decreased with an increase of the raw material mass ration. The reason for the decrease of phase change latent heat is that in the prepared composite SLPCMs, the Al-Si alloy was used as SLPCM and Al_2O_3 as shell layer, and the melting or crystallization latent heat of composite SLPCMs was derived from the melting or crystallization of Al-Si alloy. Thus, for a given mass of composite SLPCMs, the lower the Al_2O_3 shell content is, the higher will be the core Al-Si alloy content and the phase change latent heat value.

Based on the above analysis results, it can be concluded that with an increase in the raw material mass ratio, the average particle diameter and phase change latent heat of the prepared composite SLPCMs decreased. Therefore, the sample $CP_{A\text{-}8B\text{-}0.07}$ with the average particle diameter of 112.6 μm exhibited the highest melting latent heat (278.2 J/g), which can be expected to apply in stationary conditions. Compared with the samples $CP_{A\text{-}8B\text{-}0.07}$ and $CP_{A\text{-}8B\text{-}0.10}$, the sample $CP_{A\text{-}8B\text{-}0.13}$ exhibited the lowest melting latent heat (209.5 J/g). However, the sample $CP_{A\text{-}8B\text{-}0.13}$ with the average particle diameter of 39.3 μm exhibited good liquidity, which can be used as heat transfer fluid in thermal energy storage mobile applications.

3.3. Thermal conduction property of the prepared composite SLPCMs

Thermal conductivity is an important indicator to evaluate the heat transfer efficiency of phase change thermal energy storage materials. Table 3 lists the thermal conductivity of $CP_{A\text{-}0B\text{-}0.13}$, $CP_{A\text{-}8B\text{-}0.07}$, $CP_{A\text{-}8B\text{-}0.10}$ and $CP_{A\text{-}8B\text{-}0.13}$. As given in Table 3, the thermal conductivity of the prepared composite SLPCMs is ranging from 2.068 $W(mK)^{-1}$ to 2.966 $W(mK)^{-1}$. Moreover, the thermal conductivity of the prepared composite SLPCMs decreased with the increase of the raw material mass ratio, which is caused by that for a given mass of composite SLPCMs, the Al_2O_3 content increased as the increase of the raw material mass ration, while the content of Al-Si alloy decreased. Proverbially, the thermal conductivity of Al-Si alloy is higher than that of Al_2O_3. It should be emphasized that the thermal conductivity of the prepared composite SLPCMs is at an advanced level even compared with some high-temperature SLPCMs modified by carbon materials [45,46].

Table 3
Thermal conductivity of samples $CP_{A\text{-}0B\text{-}0.13}$, $CP_{A\text{-}8B\text{-}0.07}$, $CP_{A\text{-}8B\text{-}0.10}$ and $CP_{A\text{-}8B\text{-}0.13}$.

Samples	$CP_{A\text{-}0B\text{-}0.13}$	$CP_{A\text{-}8B\text{-}0.07}$	$CP_{A\text{-}8B\text{-}0.10}$	$CP_{A\text{-}8B\text{-}0.13}$
Thermal conductivity [W (m K)$^{-1}$]	2.966 ± 1.165 *10^{-3}	2.734 ± 3.810 *10^{-3}	2.402 ± 2.926 *10^{-3}	2.068 ± 3.106 *10^{-3}

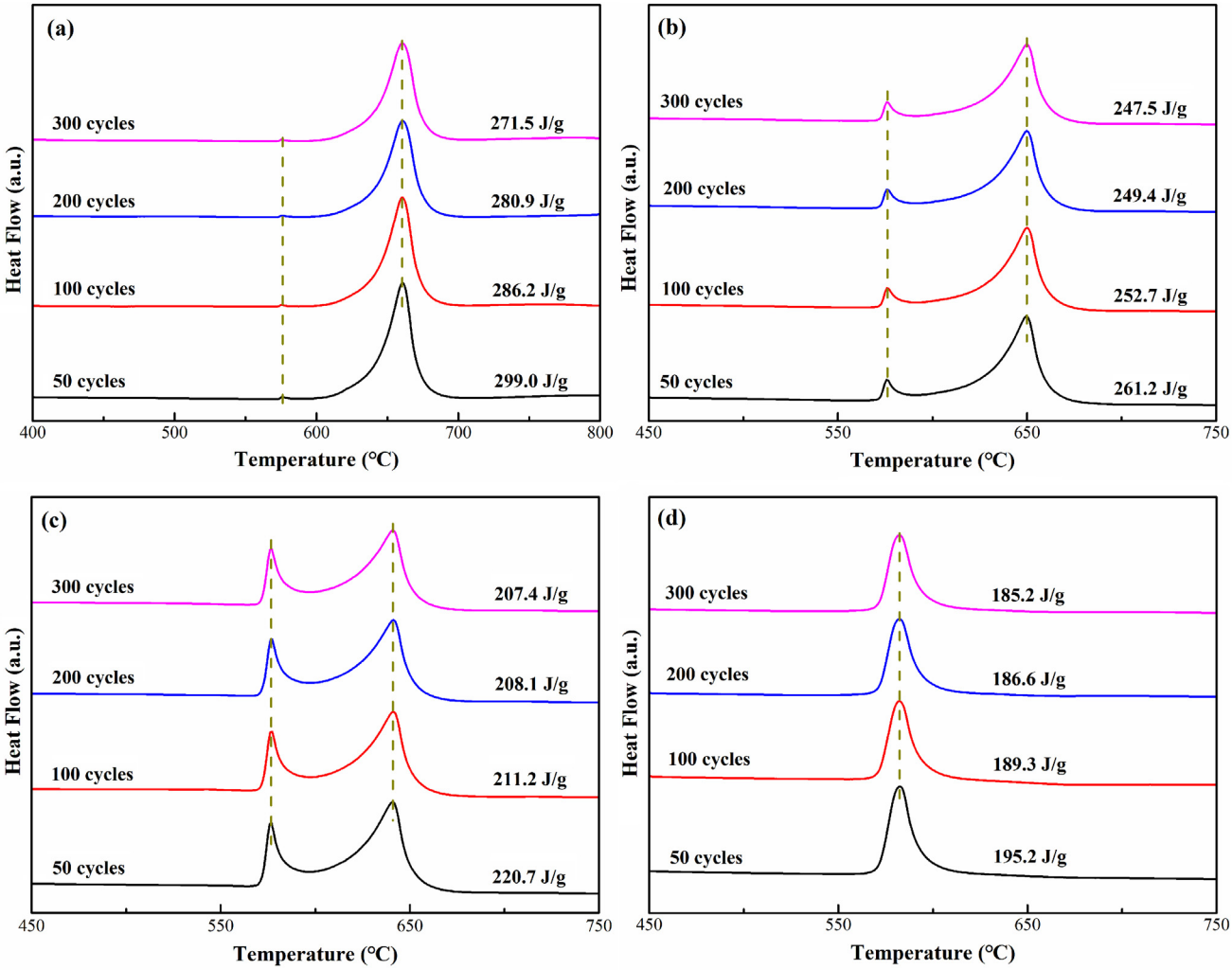

Fig. 7. DSC heating curves of (a) $CP_{A\text{-}0B\text{-}0.13}$; (b) $CP_{A\text{-}8B\text{-}0.07}$; (c) $CP_{A\text{-}8B\text{-}0.10}$ and (d) $CP_{A\text{-}8B\text{-}0.13}$ after different thermal cycles.

3.4. Thermal cycling stability property of the prepared composite SLPCMs

The DSC heating curves of $CP_{A\text{-}0B\text{-}0.13}$, $CP_{A\text{-}8B\text{-}0.07}$, $CP_{A\text{-}8B\text{-}0.10}$ and $CP_{A\text{-}8B\text{-}0.13}$ after different thermal cycles are shown in Fig. 7, and the corresponding melting latent heat is given in Table 4. As seen from Fig. 7, there was no significant change in the melting temperature of $CP_{A\text{-}0B\text{-}0.13}$, $CP_{A\text{-}8B\text{-}0.07}$, $CP_{A\text{-}8B\text{-}0.10}$ and $CP_{A\text{-}8B\text{-}0.13}$ after 300 thermal cycles, which suggests that the prepared composite SLPCMs exhibited a great thermal stability. However, after 300 thermal cycles, the melting latent heat of the prepared composite SLPCMs reduced. The reason for the decrease of latent heat during the thermal cycling can be described as follows. According to the analysis results of SEM, EDS and XRD, the prepared composite SLPCMs particles were generally well-encapsulated by Al_2O_3 shell, but it is unavoidable that a handful of samples were not well-encapsulated or cracked during the thermal cycling. Thus, the Al-based alloy exposed to the particle surface would be oxidized during the thermal cycling conducted in air, thereby resulting in the decrease of Al-based alloy SLPCM content and melting latent heat value in the prepared composite SLPCMs. According to Table 4, the total decrease in the melting latent heat of samples $CP_{A\text{-}0B\text{-}0.13}$, $CP_{A\text{-}8B\text{-}0.07}$, $CP_{A\text{-}8B\text{-}0.10}$ and $CP_{A\text{-}8B\text{-}0.13}$ was 58.1 J/g, 30.7 J/g, 31.7 J/g and 24.3 J/g, respectively. It can be clearly observed that the reduction of melting latent heat in the prepared Al-Si/Bi/Al_2O_3 (samples $CP_{A\text{-}8B\text{-}0.07}$, $CP_{A\text{-}8B\text{-}0.10}$ and $CP_{A\text{-}8B\text{-}0.13}$) after 300 thermal cycles was lower than that in the prepared Al-Si/Al_2O_3 (sample $CP_{A\text{-}0B\text{-}0.13}$), suggesting that the core/void/shell Al-Si/Bi/Al_2O_3 exhibited a better thermal stability than the core/shell Al-Si/Al_2O_3. The improvement in the thermal stability of Al-Si/Bi/Al_2O_3 can be ascribed to the formation of void layer. Since the void layer of the prepared composite SLPCMs could provide the space for the volume expansion of the core SLPCM during the phase transition process, the thermal stress on the shell layer caused by the volume expansion of the SLPCM melt was effectively alleviated. Thus, the prepared Al-Si/Bi/Al_2O_3 composite SLPCMs have an excellent thermal stability and reusable performance.

Table 4
Melting latent heat of samples $CP_{A\text{-}0B\text{-}0.13}$, $CP_{A\text{-}8B\text{-}0.07}$, $CP_{A\text{-}8B\text{-}0.10}$ and $CP_{A\text{-}8B\text{-}0.13}$ after 50, 100, 200 and 300 thermal cycles.

Samples	50 cycles (J/g)	100 cycles (J/g)	200 cycles (J/g)	300 cycles (J/g)	Total loss amount (J/g)
$CP_{A\text{-}0B\text{-}0.13}$	299.0	286.2	280.9	271.5	58.1
$CP_{A\text{-}8B\text{-}0.07}$	261.2	252.7	249.4	247.5	30.7
$CP_{A\text{-}8B\text{-}0.10}$	220.7	211.2	208.1	207.4	31.7
$CP_{A\text{-}8B\text{-}0.13}$	195.2	189.3	186.6	185.2	24.3

Moreover, the XRD patterns of the prepared Al-Si/Bi/Al_2O_3 (e.g. sample $CP_{A\text{-}8B\text{-}0.13}$) after 100, 200 and 300 cycles are shown in Fig. 8 (a). As seen from Fig. 8 (a), the phase composition of $CP_{A\text{-}8B\text{-}0.13}$ did not change significantly after different thermal cycles and was mainly composed of Al, Bi, Al_2O_3 and Si. Moreover, the diffraction peaks of Bi_2O_3 were not observed in Fig. 8 (a), indicating that the Bi was mostly likely distributed in the core of particle rather than the shell [47,48]. If

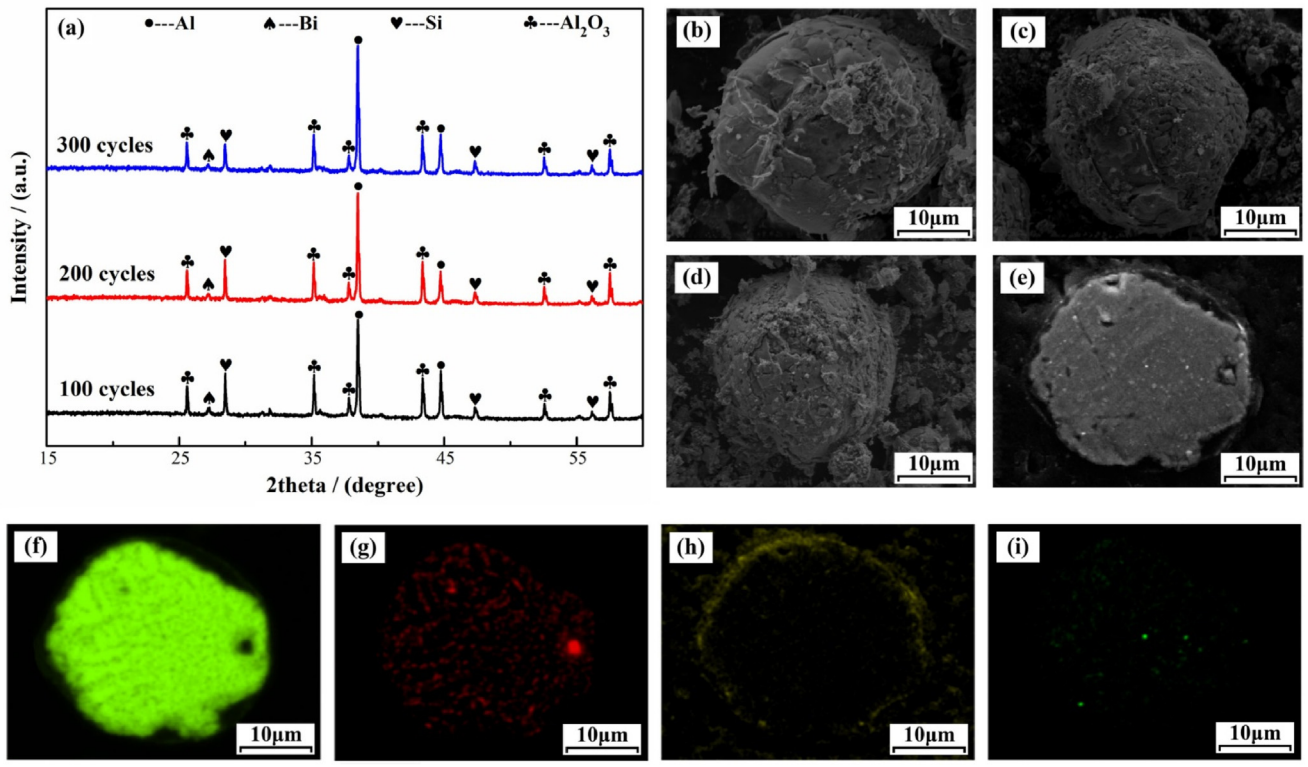

Fig. 8. (a) XRD patterns of $CP_{A\text{-}8B\text{-}0.13}$ after 100, 200 and 300 cycles; SEM images of $CP_{A\text{-}8B\text{-}0.13}$ after (b) 100 cycles; (c) 200 cycles; (d) 300 cycles; (e) SEM image of cross-sectional $CP_{A\text{-}8B\text{-}0.13}$ after 300 cycles and (f) Al element mapping; (g) Si element mapping; (h) O element mapping; (i) Bi element mapping.

the Bi was distributed in the shell, it would be inevitably oxidized to Bi_2O_3 during the thermal cycling conducted in air. The SEM images of $CP_{A\text{-}8B\text{-}0.13}$ after 100, 200 and 300 thermal cycles are given in Fig. 8 (b), (c) and (d), respectively. It was detected from Fig. 8 (b-d) that the sample $CP_{A\text{-}8B\text{-}0.13}$ after different thermal cycles still possessed a relatively dense and complete shell layer. The SEM image and elemental mappings of cross-sectional $CP_{A\text{-}8B\text{-}0.13}$ after 300 thermal cycles, as shown in Fig. 8 (e-i), further proved the above analysis results. Additionally, the structure stability of $CP_{A\text{-}0B\text{-}0.13}$, $CP_{A\text{-}8B\text{-}0.07}$ and $CP_{A\text{-}8B\text{-}0.10}$ after 300 thermal cycles was also investigated, and the similar results were obtained (as given in Fig.S10-S12).

4. Conclusions

In this study, the Al/Bi alloy powders produced by gas atomization method were used as the starting material to prepare novel core(=Al-Si/Bi)/void/shell($=Al_2O_3$) composite SLPCMs. The low melting point phase Bi mainly played two roles in the preparation process of composite SLPCMs: (1) Served as an additive to improve the activation of the alloy powders and promoted the formation of precursor shell on the Al/Bi surface; (2) Served as the template to produce the void layer that provided a space buffer to alleviate the volume expansion of core SLPCM. The thermal cycling test results showed that after 300 thermal cycles, the melting latent heat reduction of the core(=Al-Si/Bi)/void/shell($=Al_2O_3$) composite SLPCMs (24.3–31.7 J/g) was much less than that of the core(=Al-Si)/shell($=Al_2O_3$) composite SLPCM (58.1 J/g). Moreover, the particle diameter distribution, DSC and thermal conductivity analysis results indicated that the prepared Al-Si/Bi/Al_2O_3 composite SLPCMs presented an adjustable average particle diameter (39.3 μm to 112.6 μm) and melting temperature (571.9 °C to 631.9 °C), excellent thermal storage capacity (209.5 J/g to 278.2 J/g), and relatively high thermal conductivity [2.068 $W(mK)^{-1}$ to 2.966 $W(mK)^{-1}$]. Overall, this core(=Al-Si/Bi)/void/shell($=Al_2O_3$) composite represents a new paradigm for PCMs that can be applied to improve the energy efficiency of various industrial systems.

Declaration of interests

None

Acknowledgment

This study was supported by the National Natural Science Foundation of China (Grant No. 51771158) and Development and Reform Commission of Shenzhen Municipality.

Appendix A. Supplementary data

Supplementary data to this article can be found online at https://doi.org/10.1016/j.cej.2019.123539.

References

[1] A. Sharma, V. Tyagi, C. Chen, D. Buddhi, Review on thermal energy storage with phase change materials and applications, Renew. Sust. Energy Rev. 13 (2009) 318–345.
[2] F. Xue, Y. Lu, X. Qi, J. Yang, Y. Wang, Melamine foam-temperature grapheme nanoplatelet framework toward phase change materials with multiple energy conversion abilities, Chem. Eng. J. 365 (2019) 20–29.
[3] H. Wei, X. Li, Preparation and characterization of a lauric-myristic-stearic acid/Al_2O_3-loaded expanded vermiculite composite phase change material with enhanced thermal conductivity, Sol. Energy Mater. Sol. Cells 166 (2017) 1–8.
[4] S. Chu, A. Majumdar, Opportunities and challenges for a sustainable energy future, Nature 488 (2012) 294–303.
[5] C. Lai, S. Lin, Y. Chu, C. Chang, Y. Chueh, Tunable endothermic plateau for enhancing thermal energy storage obtained using binary metal alloy particles, Nano Energy 25 (2016) 218–224.
[6] X. Huang, X. Chen, A. Li, D. Atinafu, H. Gao, W. Dong, G. Wang, Shape-stabilized phase change materials based on porous supports for thermal energy storage applications, Chem. Eng. J. 356 (2019) 641–661.
[7] X. Chen, H. Gao, L. Xing, W. Dong, A. Li, P. Cheng, P. Liu, G. Wang, Nanoconfinement effects of N-doped hierarchical carbon on thermal behaviors of organic phase change materials, Energy Storage Mater. 18 (2019) 280–288.

[8] S. Khare, M. Dell Amico, C. Knight, S. McGarry, Selection of materials for high temperature latent heat energy storage, Sol. Energy Mater. Sol. Cells 107 (2012) 20–27.

[9] M. Liu, J. Gomez, N. Turchi, H. Tay, W. Saman, F. Bruno, Determination of thermo-physical properties and stability testing of high-temperature phase-change materials for CSP applications, Sol. Energy Mater. Sol. Cells 139 (2015) 110–116.

[10] H. Tian, W. Wang, J. Ding, X. Wei, C. Huang, Preparation of binary eutectic chloride/expanded graphite as high-temperature thermal energy storage materials, Sol. Energy Mater. Sol. Cells 149 (2016) 187–194.

[11] S. Guillot, A. Faik, A. Rakhmatullin, J. Lambert, E. Veron, P. Echegut, Corrosion effects between molten salts and thermal storage materials for concentrated solar power plants, Appl. Energy 94 (2012) 174–181.

[12] N. Gokon, S. Nakamura, T. Hatamachi, T. Kodama, Steam reforming of methane using double-walled reformer tubes containing high-temperature thermal storage Na_2CO_3/MgO composites for solar fuel production, Energy 68 (2014) 773–782.

[13] T. Nomura, N. Sheng, C. Zhu, G. Saito, D. Hanzaki, T. Hiraki, T. Akiyama, Microencapsulated phase change materials with high heat capacity and high cyclic durability for high-temperature thermal energy storage and transportation, Appl. Energy 188 (2017) 9–18.

[14] M. Liu, W. Saman, F. Bruno, Review on storage materials and thermal performance enhancement techniques for high temperature phase change thermal storage systems, Renew. Sust. Energy Rev. 16 (2012) 2118–2132.

[15] R. Fukahori, T. Nomura, C. Zhu, N. Sheng, N. Okinaka, T. Akiyama, Macroencapsulation of metallic phase change material using cylindrical-type ceramic containers for high-temperature thermal energy storage, Appl. Energy 170 (2016) 324–328.

[16] A. Fernandez, G. Barreneche, M. Belusko, M. Segarra, F. Bruno, L. Gabeza, Considerations for the use of metal alloys as phase change materials for high temperature applications, Sol. Energy Mater. Sol. Cells 171 (2017) 275–281.

[17] M. Kenisarin, High-temperature phase change materials for thermal energy storage, Renew. Sust. Energy Rev. 14 (2010) 955–970.

[18] N. Sheng, C. Zhu, G. Saito, T. Hiraki, M. Haka, Y. Hasegawa, H. Sakai, T. Akiyama, T. Nomura, Development of a microencapsulated Al-Si phase change material with high-temperature thermal stability and durability over 3000 cycles, J. Mater. Sci. A 6 (2018) 18143–18153.

[19] F. He, G. Song, X. He, C. Sui, M. Li, Structural and phase change characteristics of inorganic microencapsulated core/shell Al-Si/Al_2O_3 micro-particles during thermal cycling, Ceram. Int. 41 (2015) 10689–10696.

[20] B. Li, T. Liu, L. Hu, Y. Wang, S. Nie, Facile preparation and adjustable thermal property of stearic acid-graphene oxide composite as shape-stabilized phase change material, Chem. Eng. J. 215 (2013) 819–826.

[21] J. Wang, M. Yang, Y. Lu, Z. Jin, L. Tan, H. Gao, S. Fan, W. Dong, G. Wang, Surface functionalization engineering driven crystallization behavior of polyethylene glycol confined in mesoporous silica for shape-stabilized phase change materials, Nano Energy 19 (2016) 78–87.

[22] H. Gao, J. Wang, X. Chen, G. Wang, X. Huang, A. Li, W. Dong, Nanoconfinement effects on thermal properties of nanoporous shape-stabilized composite PCMs: A review, Nano Energy 53 (2018) 769–797.

[23] G. Li, Z. Tang, Noble metal nanoparticle@metal oxide core/yolk-shell nanostructures as catalysts: recent progress and perspective, Nanoscale 6 (2014) 3995–4011.

[24] L. Soler, J. Macanas, M. Munoz, J. Casado, Synergistic hydrogen generation from aluminum, aluminum alloys and sodium borohydride in aqueous solutions, J. Hydrogen Energy 32 (2007) 4702–4710.

[25] C. Wang, X. Liu, I. Ohnuma, R. Kainuma, K. Ishida, Formation of immiscible alloy powders with egg-type microstructure, Science 297 (2002) 990–993.

[26] R. Shi, C. Wang, D. Wheeler, X. Liu, Y, Wang, Formation mechanisms of self-organized core/shell and core/shell/corona microstructures in liquid droplets of immiscible alloys, Acta Metall. 61 (2013) 1229–1243.

[27] Y. Yu, Y. Takaku, M. Nagasako, C. Wang, X. Liu, R. Kainuma, K. Ishida, Liquid-immiscibility-induced formation of micron-scale crystalline/amorphous composite powder, Intermetallics 25 (2012) 95–100.

[28] C. Wang, X. Liu, R. Shi, Design and formation mechanism of self-organized core/shell structure composite powder in immiscible liquid system, Appl. Phys. Lett. 91 (2007) 141904–141907.

[29] C. Wang, Y. Liu, H. Liu, T. Yang, X. Chen, S. Yang, X. Liu, A Novel Self-Assembling Al-based Composite Powder with High Hydrogen Generation Efficiency, Sci. Rep. 5 (2015) 17428–17433.

[30] Y. Liu, X. Liu, X. Chen, S. Yang, C. Wang, Hydrogen generation from hydrolysis of activated Al-Bi, Al-Sn powders prepared by gas atomization method, Int. J. Hydrogen Energy 42 (2017) 10943–10951.

[31] K. Vrancken, E. Casteleyn, K. Possemiers, V. Van der, E. Vansant, Modelling of the reaction-phase interaction of γ-Aminopropyltriethoxysilane with silica, J. Chem. Soc. 89 (1993) 2037-2040.

[32] K. Vrancken, K. Possemiers, V. Van der, E. Vansant, Surface modification of silica gels with aminoorganosilanes, Colloid Surface A 98 (1995) 235-341.

[33] G. Wang, F. Yan, Z. Teng, W. Yang, T. Li, The surface modification of silica with APTS, Prog. Chem. 18 (2006) 238–345.

[34] M. Fan, F. Xu, L. Sun, Hydrogen generation by hydrolysis reaction of ball-milled Al-Bi alloys, Energy Fuel. 21 (2007) 2294–2298.

[35] C. Hessel, E. Henderson, J. Veinot, Hydrogen silsesquioxane: a molecular precursor for nanocrystalline Si-SiO_2 composites and freestanding hydride-surface-terminated silicon nanoparticles, Chem. Mater. 18 (2006) 6139–6146.

[36] S. Hong, M. Lee, S. Park, G. Lee, Synthesis of nanosized TiO_2/SiO_2 particles in the microemulsion and their photocatalytic activity on the decomposition of p-nitrophenol, Catal. Today 87 (2003) 99–105.

[37] J. Lin, C. Ma, Thermal degradation of phenolic resin/silica hybrid ceramers, Polym. Degrad. Stabil. 69 (2000) 229–235.

[38] J. Tong, X. Han, S. Wang, X. Jiang, Evaluation of structure characteristics of huadian oil shale kerogen using direct techniques (solid-state 13C NMR, XPS, FT-IR, and XRD), Energy Fuels 25 (2011) 4006–4013.

[39] F. He, C. Sui, X. He, M. Li, Inorganic microcapsulated core-shell structure of Al-Si alloy micro-particles with silane coupling agent, Ceram. Int. 40 (2014) 6865–6874.

[40] N. Lin, Y. Han, J. Zhou, K. Zhang, T. Xu, Y. Zhu, Y. Qian, A low temperature molten salt process for aluminothermic reduction of silicon oxides to crystalline Si for Li-ion batteries, Energy Environ. Sci. 8 (2015) 3187–3191.

[41] H. Wang, Y. Li, T. Zhu, S. Sang, Q. Wang, Microstructures and mechanical properties of Al_2O_3-C refractories with addition of microcrystalline graphite, Ceram. Int. 40 (2014) 11139–11148.

[42] T. Chanadee, Experimental studies on self-propagating high-temperature synthesis of Si-SiC composite from reactants of SiO_2 derived from corn cob ash/C/Mg, J. Aust. Ceram. Soc. 53 (2017) 245–252.

[43] N. Yoshikawa, A. Kikuchi, S. Taniguchi, Anomalous temperature dependence of the growth rate of the reaction layer between silica and molten aluminum, J. Am. Ceram. Soc. 85 (2002) 1827–1834.

[44] T. Omori, J. Sato, K. Shinagawa, I. Ohnuma, K. Oikawa, R. Kainuma, K. Ishida, Experimental determination of phase equilibria in the Co-Cr-Ni system, J. Phase Equilib. Diff. 35 (2014) 178–185.

[45] K. Li, X. Cheng, N. Li, X. Zhu, Y. Wei, K. Zhai, H. Wang, A yolk/shell strategy for designing hybrid phase change materials for heat management in catalytic reactions, J. Mater. Sci. A 5 (2017) 24232–24246.

[46] P. Zhang, X. Xiao, Z. Ma, A review of the composite phase change materials: Fabrication, characterization, mathematical modeling and application to performance enhancement, Appl. Energy 165 (2016) 472–510.

[47] H. Cheng, B. Huang, J. Lu, Z. Wang, B. Xu, X. Qin, X. Zhang, Y. Dai, Synergistic effect of crystal and electronic structures on the visible-light-driven photocatalytic performances of Bi_2O_3 polymorphs, Phys. Chem. Chem. Phys. 12 (2010) 15468–15475.

[48] J. Hou, C. Yang, Z. Wang, W. Zhou, S. Jiao, H. Zhu, In situ synthesis of α-β phase heterojunction on Bi_2O_3 nanowires with exception visible-light photocatalytic performance, Appl. Catal. B: Environ. 142 (2013) 504–511.